Thermal Predictions of the AGR-3/4 Experiment With Time-Varying Gas Gaps

Grant L. Hawkes[1]
Idaho National Laboratory,
2525 Fremont, MS 3870,
Idaho Falls, ID 83415
e-mail: Grant.Hawkes@inl.gov

James W. Sterbentz
Idaho National Laboratory,
2525 Fremont, MS 3870,
Idaho Falls, ID 83415
e-mail: James.Sterbentz@inl.gov

John T. Maki
Idaho National Laboratory,
2525 Fremont, MS 3870,
Idaho Falls, ID 83415
e-mail: John.Maki@inl.gov

A thermal analysis was performed for the Advanced Gas Reactor test experiment (AGR-3/4) with time-varying gas gaps. The experiment was irradiated at the Advanced Test Reactor (ATR) at the Idaho National Laboratory (INL). Several fuel irradiation experiments are planned for the AGR Fuel Development and Qualification Program that supports the development of the Very-High-Temperature Gas-Cooled Reactor (VHTR) under the Next-Generation Nuclear Plant (NGNP) project. AGR-3/4 combines two tests in a series of planned AGR experiments to test tristructural-isotropic (TRISO)-coated, low-enriched uranium oxy-carbide fuel. Forty-eight TRISO-fueled compacts were inserted into 12 separate capsules for the experiment (four compacts per capsule). The purpose of this analysis was to calculate the temperatures of each compact and graphite layer to obtain daily average temperatures using time (fast neutron fluence)-varying gas gaps and to compare with experimentally measured thermocouple data. A finite-element heat transfer model was created for each capsule using the commercial code ABAQUS. Model results are compared to thermocouple data taken during the experiment. [DOI: 10.1115/1.4030046]

Keywords: TRISO-fueled compacts, irradiation testing in ATR, thermal modeling, gas gaps varying with neutron fluence, high-temperature gas reactors

1 Introduction

The AGR-1 and AGR-2 experiments irradiated in the Advanced Test Reactor (ATR) have previously been modeled for daily thermal evaluation in Refs. [1] and [2]. The author discusses similar topics in these references to this article, such as variable gas gaps, mesh sensitivity, thermal conductivity varying with fast neutron fluence, and daily thermal heat rates imported from physics analysis. These first two experiments were shake-down tests for the TRISO fuel particles in compacts.

The AGR-3/4 experiment is composed of 12 individual capsules, approximately 0.06985 m (2.75 in.) diameter by 0.1016 m (4.00 in.) tall, stacked on top of each other to form the test train. Each capsule contains four TRISO-particle compacts that are approximately 0.0127 m (0.5 in.) diameter by 0.0127 m (0.5 in.) long. The compacts are composed of TRISO fuel particles bound together by a carbon matrix. Each compact contains approximately 4150 fissile particles (36 vol% particle packing fraction). Each capsule is supplied with a flowing helium/neon gas mixture to control the test temperature and sweep any fission gases that are released to the fission product monitoring system. Temperature control is accomplished by adjusting the gas mixture ratio of the two gases (helium and neon) with differing thermal conductivities in the gas gaps.

The AGR-3/4 experiment was placed in the north-east flux trap position in the ATR core as shown in Fig. 1. An axial view of two of the 12 capsules is shown in Fig. 2. Four through tubes carry thermocouples (TCs) and gas lines to each individual capsule. All 12 capsules have their own gas mixture and fission product gas return line. Figure 2 also shows the arrangement of how the capsules are stacked together to form the experiment train. Each capsule has a fuel compact in the center surrounded by three graphitic annuli as shown in Fig. 3. Symmetry may not be assumed as the heat rates vary azimuthally for each graphite layer. The graphite annuli proceeding from the compact out are the matrix ring (inside), graphite sleeve, and graphite sink (outside). The largest gas gaps are shown on the outside and inside of the graphite sink. Gas gaps for the two innermost gaps are very small and not perceptible in Fig. 3. Each of these four components is designed to operate at a specified temperature in all 12 capsules. Through tubes containing gas lines and TC wires are displayed in Fig. 3. Four temperature control gas gaps separate these components for a total of 48 gas gaps in the entire test train. Reactor coolant water flows on the outside of the stainless steel capsule shell.

The commercial finite-element heat transfer code ABAQUS [3] was used for this analysis. The ABAQUS model has a direct volume-for-volume correlation with the physics model. A similar physics model is discussed in Ref. [4] for the heating of the compacts (each compact is evenly and axially divided into two equal parts). The goal of these predictions is to be able to adjust the TC set points as the fuel burns during the experiment so as to maintain constant fuel temperature.

2 Numerical Model and Discussion

A cutaway rendering of a typical capsule is shown on the left side of Fig. 4. One of the main goals of this experiment was to make the bulk of the heat from the compacts flow radially out of the capsule instead of axially out of the ends of the capsule. Zirconia, grafoil, and graphite felt insulators are placed on the top and bottom of each capsule shown in Fig. 4. The finite-element mesh with a cutaway view colored by different materials of the entire model is shown on the right side of Fig. 4. A Cartesian coordinate system is appropriate for this model because of the three-dimensionality of the heat flow. Approximately, 400,000 eight-noded hexahedral brick elements were exclusively used in all 12 capsule models. Several mesh convergence studies [1,2] have been performed on the mesh. Identical agreement for this mesh and a mesh with twice as many elements in each direction was obtained. The exclusive use of eight-noded hexahedral brick elements ensures good numerical accuracy for this type of heat conduction model as discussed in

[1]Corresponding author.

Manuscript received January 14, 2015; final manuscript received March 10, 2015; published online September 3, 2015. Assoc. Editor: Jovica R. Riznic.

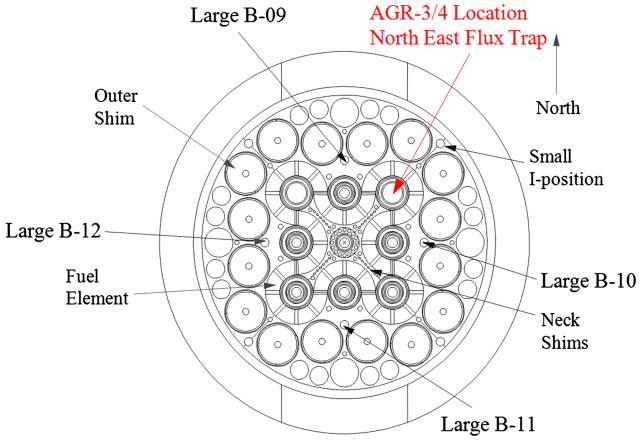

Fig. 1 ATR core cross section showing the north-east flux trap position containing the AGR-3/4 experiment

Refs. [1] and [2]. The finite-element models have a mesh density in the radial direction of approximately 38 finite elements per inch with a characteristic length of 0.965 mm (0.038 in.). The gap conductance model was implemented for the outside three gas gaps, while the innermost gas gap had hexagonal brick elements. This innermost gap was modeled with brick elements as all the capsules had the same gas gap. As only one basic mesh was created and propagated to the other 11 capsules, various gas gap conductivities and gap conductances were implemented by taking into account each individual gap dimension. The top and bottom of each model were assumed to be adiabatic. This implies that we are ignoring radiation heat transfer from the top of one capsule to the bottom of the one above. The gas gap between capsules is more than 0.0127 m (0.5 in.).

The fuel compact thermal conductivity was taken from correlations presented from Gontard and Nabielek in Ref. [5], which gives correlations for conductivity, taking into account temperature, temperature of heat treatment, neutron fluence, and TRISO-coated particle packing fraction (where packing fraction is defined as the total volume of particles divided by the total volume of the compact).

In this work, the convention used to quantify neutron damage to a material is neutron fast fluence (n/m^2, $E_n > 0.18$ MeV), where E_n is the neutron energy, yet in the work by Gontard and Nabielek, the unit used was the dido nickel equivalent (DNE). In order to convert from the DNE convention to the fast fluence >0.18 MeV, the following conversion was used

$$\Gamma_{>0.18\ \mathrm{MeV}} = 1.52\Gamma_{\mathrm{DNE}} \tag{1}$$

where Γ is neutron fluence in either the >0.18 MeV unit or DNE. The correlations in the report by Gontard and Nabielek were further adjusted to account for differences in fuel compact density. The correlations were developed for a fuel compact matrix density of 1.75 g/cm^3, whereas the compact matrix used in AGR-3/4 had a density of approximately 1.6 g/cm^3. The thermal conductivities were scaled according to the ratio of densities (0.91) in order to correct for this difference.

Figure 5 shows a three-dimensional plot of the fuel compact thermal conductivity varying with fast neutron fluence and temperature using the Chiew and Gland correlation [6] for particles in a matrix described as

$$\frac{k_e}{k_m} = \frac{1 + 2\beta\varphi + (2\beta^3 - 0.1\beta)\varphi^2 + 0.05\varphi^3 e^{4.5\beta}}{1 - \beta\varphi},$$
$$\beta = \frac{\kappa - 1}{\kappa + 2} \quad \text{and} \quad \kappa = \frac{k_p}{k_m} \tag{2}$$

where k_e is the effective thermal conductivity, k_m is the matrix thermal conductivity, k_p is the particle thermal conductivity, and φ is the particle packing fraction.

For fluences greater than 1.0×10^{25} neutrons/m^2 ($E_n > 0.18$ MeV), the conductivity increases as fluence increases for higher temperatures because of the annealing of radiation-induced defects in the material with high temperatures, while the opposite occurs at lower temperatures. The thermal conductivity of the matrix ring was taken from the fuel compacts correlation with a fuel particle packing fraction of zero. This was done since a pure matrix material conductivity was not available. A plot similar in shape to the fuel compacts, with higher conductivity, is shown in Fig. 6.

Two types of nuclear-grade graphite were used in this experiment, PCEA and IG-110. The unirradiated thermal conductivity of these two types of graphites was conducted at the Idaho National Laboratory (INL) and discussed in Ref. [7]. The effect of irradiation on the thermal conductivity of the graphite was accounted for in the analysis using the following correlation by Snead and Burchell [8]

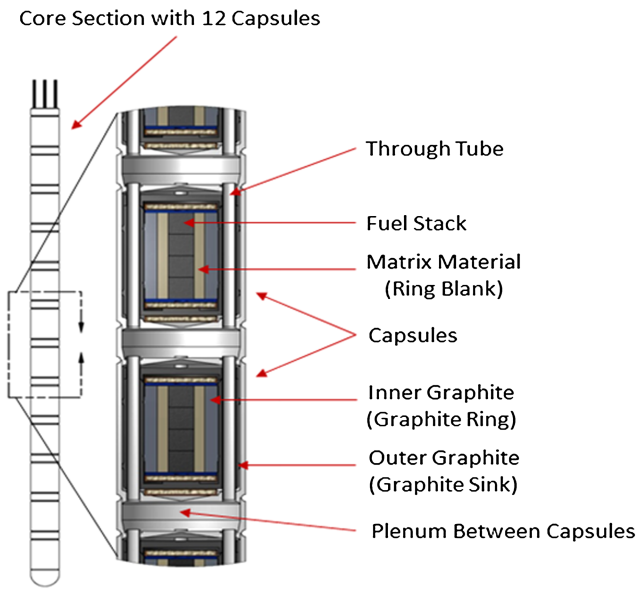

Fig. 2 ATR core cross section showing the north-east flux trap position containing the AGR-3/4 experiment

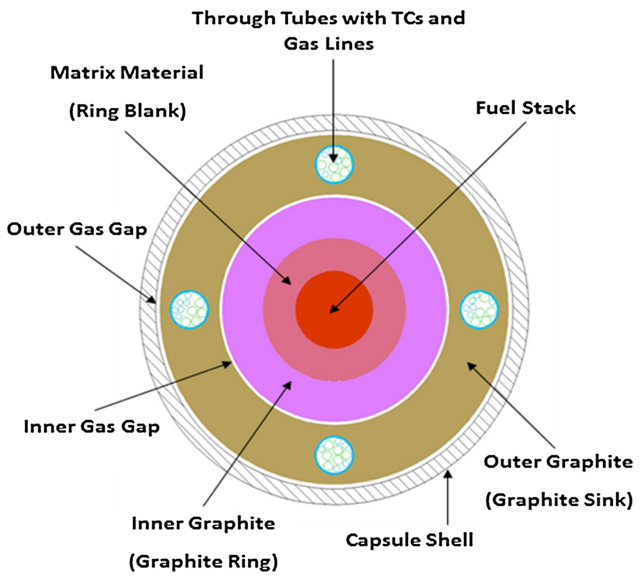

Fig. 3 Cross-sectioned view of an AGR-3/4 capsule

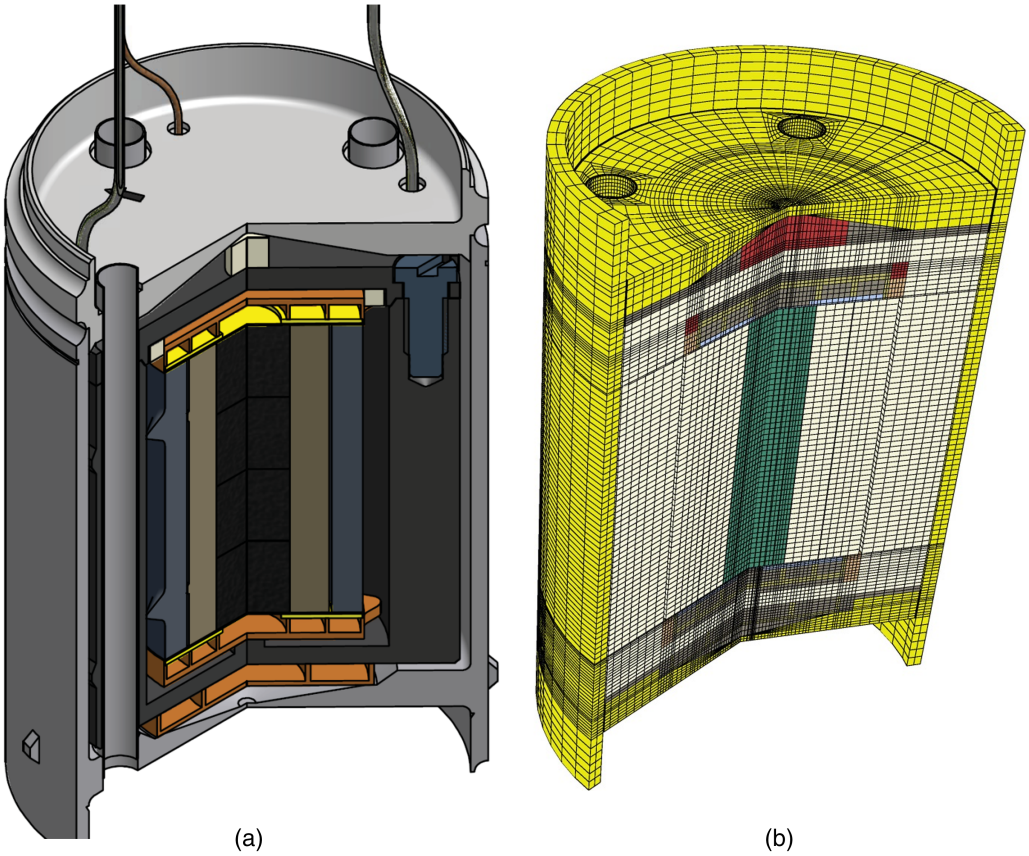

Fig. 4 Cutaway view of capsule and finite-element mesh with colored entities

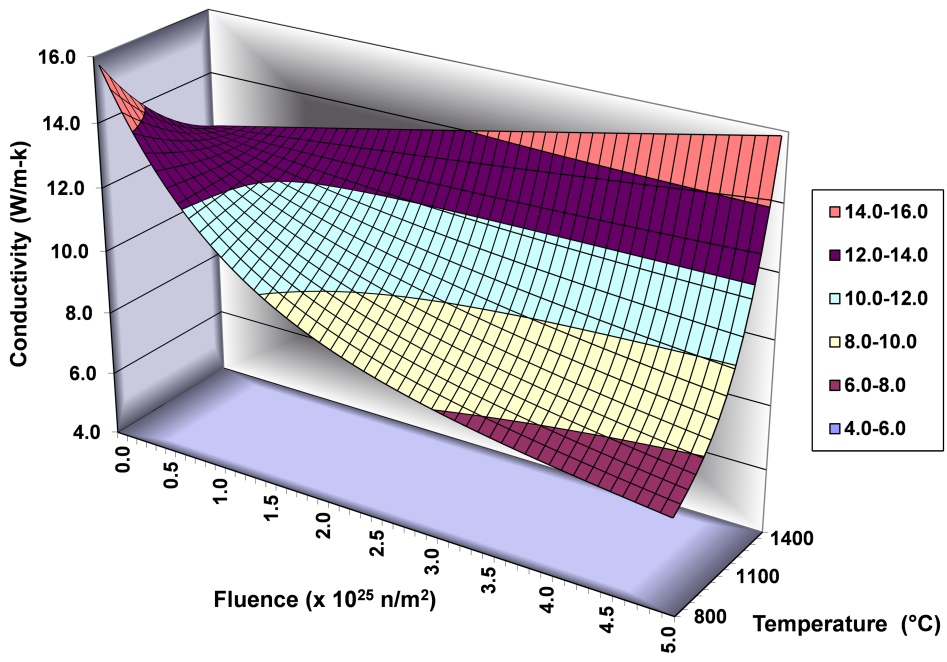

Fig. 5 Three-dimensional plot of AGR-3/4 fuel compact thermal conductivity (W/m K) varying with fluence and temperature

$$\frac{k_{\text{irr}}}{k_0} = (0.25 - 0.00017T_{\text{irr}})A\log(\text{dpa}) + 0.000683T_{\text{irr}},$$
$$A = -1.0 \tag{3}$$

where k_{irr} and k_0 are the thermal conductivities of irradiated and unirradiated graphites, respectively; T_{irr} is the irradiation temperature (°C); and dpa is the number of carbon atom displacements per atom from fast neutrons. The multiplier used to convert fast fluence

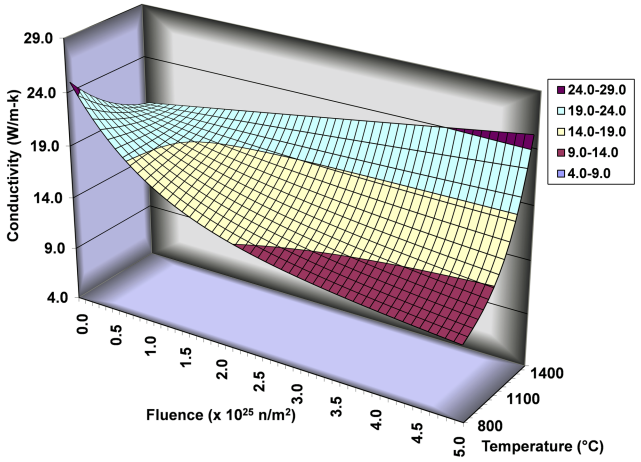

Fig. 6 Three-dimensional plot of AGR-3/4 matrix thermal conductivity (W/m K) varying with fluence and temperature

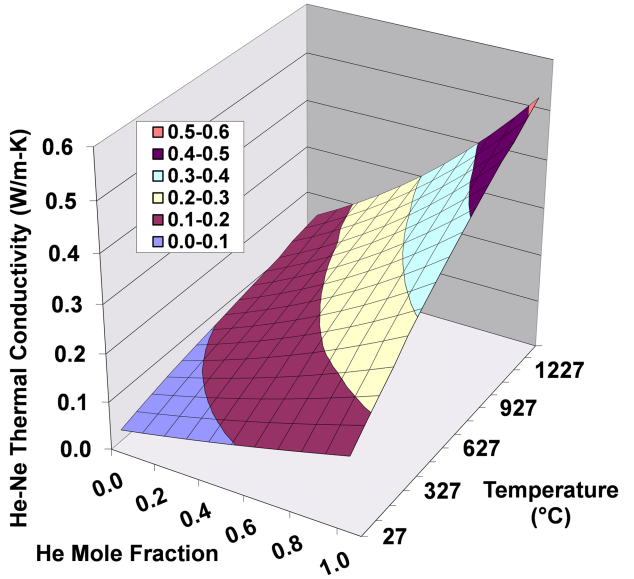

Fig. 8 Helium–neon gas thermal conductivity versus temperature and mole fraction helium

(>0.18 MeV) to dpa is 8.23×10^{-26} dpa/n/m^2 and comes from Sterbentz [9]. Figure 7 shows a three-dimensional plot of this ratio (k_{irr}/k_0) varying with dpa and temperature. This ratio of irradiated to unirradiated thermal conductivity increases for higher temperatures and decreases for higher dpa.

Figure 8 shows a plot of the helium/neon sweep gas thermal conductivity versus temperature and mole fraction of helium. The thermal conductivity increases as the helium mole fraction increases and as the temperature increases. Heat produced in the fuel compacts and graphite components is transferred through the gas gaps surrounding the compacts and components via a gap conductance model using the gap width and the conductivity of the sweep gas as discussed later. Both radiation and conduction heat transfer were considered across every gap. However, because the thermal capacitance of the sweep gas is very low (30 cm^3/ min), advection is not considered in the sweep gas. The sweep gas is modeled as being stationary. The convective heat transfer from these sweep gases would be less than 0.01% of the heat transfer across the gap because of the low density, low flow rate, and low thermal capacitance. The thermal conductivity of the sweep gas mixture was determined using a set of correlations from Brown University [10] for mixtures of noble gases.

The governing equation for steady-state heat transfer in the model is

$$0 = \frac{\partial}{\partial x}\left(k(T)\frac{\partial T}{\partial x}\right) + \frac{\partial}{\partial y}\left(k(T)\frac{\partial T}{\partial y}\right) + \frac{\partial}{\partial z}\left(k(T)\frac{\partial T}{\partial z}\right) + \dot{q} \quad (4)$$

where T is the temperature; x, y, and z are Cartesian coordinate directions; $k(T)$ is the thermal conductivity varying with temperature; and Q is the heat source. Approximately 80–85% of the heat transfer across the gas gaps is done by conduction, 15–20% by radiation across the control gas gap, and with less than 0.01% by advection. Ranges are given here to cover different temperatures for the fuel compacts.

The governing equation for radiation heat transfer across the gas gaps is

$$q_{net} = \frac{\sigma(T_1^4 - T_2^4)}{\frac{(1-\varepsilon_1)}{\varepsilon_1 A_1} + \frac{1}{A_1 F_{12}} + \frac{(1-\varepsilon_2)}{\varepsilon_2 A_2}} \quad (5)$$

where q_{net} is the net heat flux, σ is the Stephan–Boltzmann constant, T_1 and T_2 are the surface temperatures, ε_1 and ε_2 are the emissivities of surfaces 1 and 2 (postirradiation viewing of fuel compacts, graphite surfaces, and stainless steel suggests that the emissivity does not change with fluence), A_1 and A_2 are the areas of surfaces 1 and 2, and F_{12} is the view factor from surface 1 to 2. Radiation view factors for parallel disk to disk, ring to ring, and inside to outside of annulus were calculated using standard radiation view factor textbooks and implemented across each radial and axial gap. The emissivity of the graphite, grafoil, and graphite felt was assumed to be 0.9, 0.4 for stainless steel, and zirconia and zirconium at 0.5.

The neon gas fraction for each day was calculated for each capsule using average daily flow rates for helium and neon through each capsule. Graphite and fuel compact material properties vary with neutron fluence. Fluence was imported from the detailed physics daily as-run calculations. The ABAQUS Field Variable model was implemented where the neon fraction was taken as Field Variable 1, and fast neutron fluence was taken as Field Variable 2. ABAQUS thus provides a method of properties being able to vary with fields other than temperature.

The gamma/neutron heating for the various components (including the fuel compacts) was taken from the as-run physics calculations. Typical heat rates for the fuel compacts and graphite components were nominally 120 and 10 W/cm^3, respectively. The test train heat rates exhibit the typical chopped cosine profile that is distinctive of ATR.

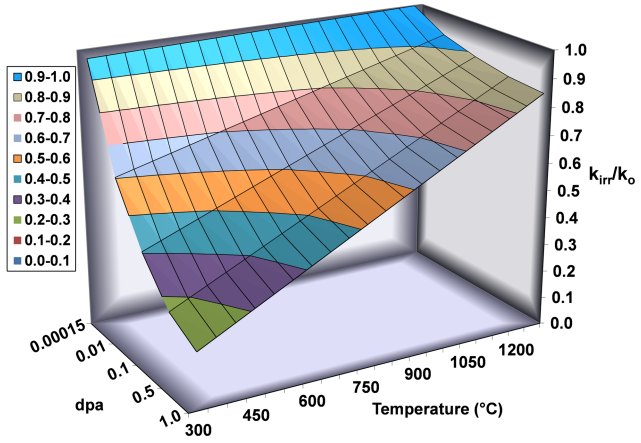

Fig. 7 Graphite thermal conductivity plot of ratio of irradiated over unirradiated varying with temperature and dpa

Table 1 Compacts, matrix, and graphite dimensional change varying with fast neutron fluence and temperature

Fast fluence (n/m^2)	AGR-1 compacts	Matrix				PCEA	IG-110
		430°C	900°C	1160°C	1430°C		
$E > 0.18$ MeV	$\Delta r/r$	$\Delta r/r$	$\Delta r/r$	$\Delta r/r$	$\Delta r/r$	$\Delta V/V$	$\Delta V/V$
0	0.0000	0.0000	0.0000	0.0000	0.0000	0.0000	0.0000
1	−0.0059	−0.0046	−0.0020	−0.0046	−0.0064	−0.0062	−0.0077
2	−0.0095	−0.0088	−0.0037	−0.0081	−0.0121	−0.0125	−0.0146
3	−0.0110	−0.0125	−0.0051	−0.0105	−0.0169	−0.0187	−0.0209
4	−0.0110	−0.0158	−0.0061	−0.0121	−0.0209	−0.0249	−0.0264
5	−0.0110	−0.0186	−0.0069	−0.0129	−0.0242	−0.0311	−0.0313
6	−0.0110	−0.0209	−0.0073	−0.0130	−0.0266	−0.0374	−0.0354
7	−0.0110	−0.0227	−0.0074	−0.0124	−0.0283	−0.0436	−0.0388
8	−0.0110	−0.0241	−0.0072	−0.0114	−0.0292	−0.0498	−0.0416

All gas gaps were modeled as changing with fast neutron fluence. This was accomplished by having the gas gap conductivity of each capsule change with neutron fluence. Fluence was set as Field Variable 2 in the ABAQUS model. The original finite-element mesh models created in ABAQUS were done with the as-built dimensions for the gas gaps. The gas gaps were assumed to be the hot gas-gap dimension, the hot gas-gap dimension and room temperature gas-gap dimension being virtually the same. Experimental data [11] obtained from the AGR-1 experiment were used for the compact dimensional change, while data from the AGC-1 experiment [12] were used for the graphite shrinkage. Matrix dimensional change data were taken from Refs. [5] and [13]. Table 1 shows the $\Delta r/r$ values obtained from measured values from the AGR-1 compact, matrix ring, and graphite in the ring and sink. The table shows two different types of graphite used in the experiment, PCEA and IG-110. This model assumes that both the inside and outside radius of the annuli shrink inward. This assumption is validated by graphite annuli measured from the Peach Bottom reactor since the 1970s [14].

Figure 9 shows the radial dimensional change as a function of fast neutron fluence for the compacts from the AGR-1 experiment. Dimensional change must be exactly zero for zero fluence. All graphites initially shrink with fluence and then eventually swell with higher values of fluence as shown in [5]. In Fig. 9, the solid triangles show the values taken from all stacks. Uncertainty values of approximately 10% are shown in [11] for experimental values in this figure. The black line shows a second-order polynomial curve-fit for the data. The straight lines connecting the solid diamonds show the values that were used in the ABAQUS model. The ABAQUS model uses the curve-fit exactly at the fluence values of 0.0, 1.0, 2.0, and 3.0 (10^{25} n/m^2) exactly, with linear interpolation in between. Compact shrinkage values remain constant above a fluence of 3.0 for this analysis, even though the curve-fit shows a slight upward trend for fluence values above 4.0. This was done for simplicity and based on data from German TRISO-fuel compact experiments since the 1980s as shown in Fig. 6.5.1 of Ref. [5]. Figure 10 shows a three-dimensional saddle-shaped plot of shrinkage for the matrix varying with temperature and fast neutron fluence. This figure shows that minimal shrinkage occurs at 900°C with more pronounced shrinkage below and above this temperature. Data for Fig. 10 come from Refs. [5] and [13]. Figure 11 shows the volumetric graphite shrinkage for the graphite ring and graphite sink varying with fast neutron fluence for IG-110 and PCEA graphites used in the experiment. These graphite shrinkage results come from the AGC-1 experiment [7]. Volumetric change data were available in this reference. To convert from volumetric to linear dimensional change, the following equation was used

$$\frac{\Delta r}{r} = \left(1 + \frac{\Delta V}{V}\right)^{\frac{1}{3}} - 1 \tag{6}$$

where r is the radius and V is the volume.

3 Results

Figures 12–18 show the results of a small sampling of the results for the first six ATR cycles 151A, 151B, 152B, 154A, 154B, and 155A. Figures 12 and 13 show temperature contours of the various components, while Fig. 14 shows a temperature history plot compared with actual TC measurements. Figures 15–18 show sensitivity to the variable gap model predictions.

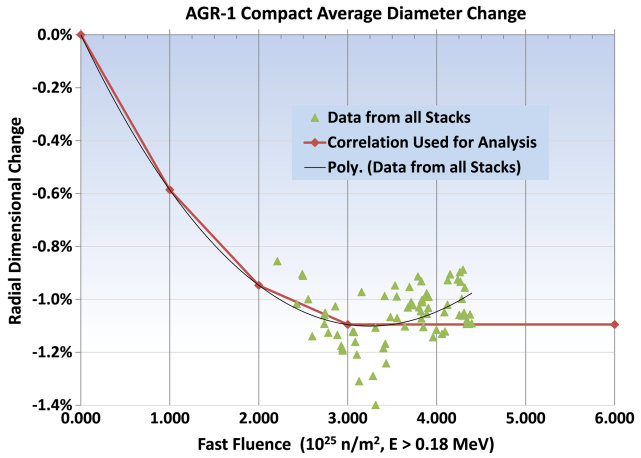

Fig. 9 AGR-1 compact dimensional change varying with fast neutron fluence

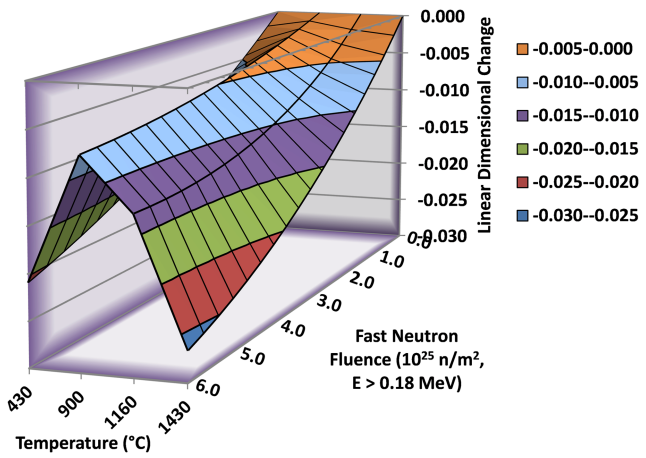

Fig. 10 Matrix shrinkage varying with fast neutron fluence and temperature

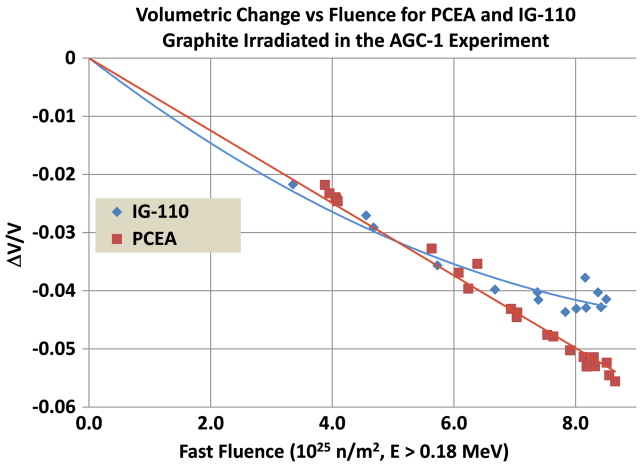

Fig. 11 Volumetric change versus fast neutron fluence for PCEA and IG-110 graphite irradiated in the AGC-1 experiment

A cutaway view of the temperature contours and mesh is shown for capsule 12 (typical) in Fig. 12. The maximum fuel compact temperature is 887°C at the center. Outside stainless steel capsule temperatures are near the temperature of the ATR primary coolant water temperature of 50°C. Gamma heating in the stainless steel end cap shows a radial temperature gradient. Several insulating materials have been placed in the model to prevent heat from transferring in the axial direction and out of the stainless steel end caps. The majority of the heat for these capsules is deposited in the fuel compacts (~1/3) and the three graphitic ring layers (~2/3).

Figure 13 shows temperature contour plots for the (*a*) fuel compacts, (*b*) matrix, (*c*) graphite ring, and (*d*) graphite sink. One goal of this experiment is to have as uniform temperature as possible in the fuel compacts and graphite rings. The majority of the compact is between 820 and 870°C as shown in Fig. 13(*a*). The very center is the hottest and outside edges are cooler as is typical for a heat-generating cylinder with heat transfer on all sides.

The matrix ring temperature contours are shown in Fig. 13(*b*). Almost the entire matrix ring is between 765 and 800°C. Similar results are shown in Fig. 13(*c*) for the graphite sleeve, with the vast majority at 748°C ± 8°C. The highest temperature in this component is at the very bottom (inside) (not shown). This occurs since the fuel compacts, matrix ring, and graphite sleeve all sit on a thin layer of grafoil that is fairly conductive, yet nonreactive with the materials contacting it. Coolest temperatures are at the top-outside corner.

Figure 13(*d*) shows the graphite sink temperature contours without the top and bottom lid. Median temperature is 495°C with minimum and maximum −15°C. Hot spots occur at the inside in the four locations where the through tubes prevent the heat from evenly transferring to the outside. Coolest temperatures are on the top-outside edges next to the through tube holes. Gamma heating for all of these annular components was implemented in the 90° segments. It appears that the azimuthal temperature variations are very small.

A temperature history plot is shown in Fig. 14 for capsule 2. The TC location for all capsules is in the north-east center of the graphite sink (fourth layer). The top panel plots the actual TC measurements for TCs 1 and 2. The horizontal axis shows the ATR cycle numbers. Each cycle represents approximately 55 effective full-power days. The vertical axis shows the temperature in °C for the TC measurements in panel 1, whereas the temperature difference (measured minus calculated) is shown in panel 2 for TC1. The higher set of triangular shaped dots in the second panel show the temperature difference for a graphite emissivity of 1.0, while the lower set of square shaped dots show emissivity of 0.9 and the heat rates lowered by a multiplying factor. This multiplying factor takes into account the amount of heat calculated to flow into the ATR coolant water in the north-east lobe. Experience has shown that multiplying by this ratio more accurately depicts temperatures in the TCs. These lower set of square shaped dots show temperature predictions of the TCs vary by less than 20°C difference. The breaks in the plot represent times during the cycles that the reactor was shut down and also at the beginning and end of each cycle. There is no simple explanation as to why some capsules predict higher and some lower. Several different inputs are used to calculate the heat rates with the MCNP code such as the driver core fuel burnup, control rods, and outer shim rotation angles. Gas gaps are changing. Vibrations may

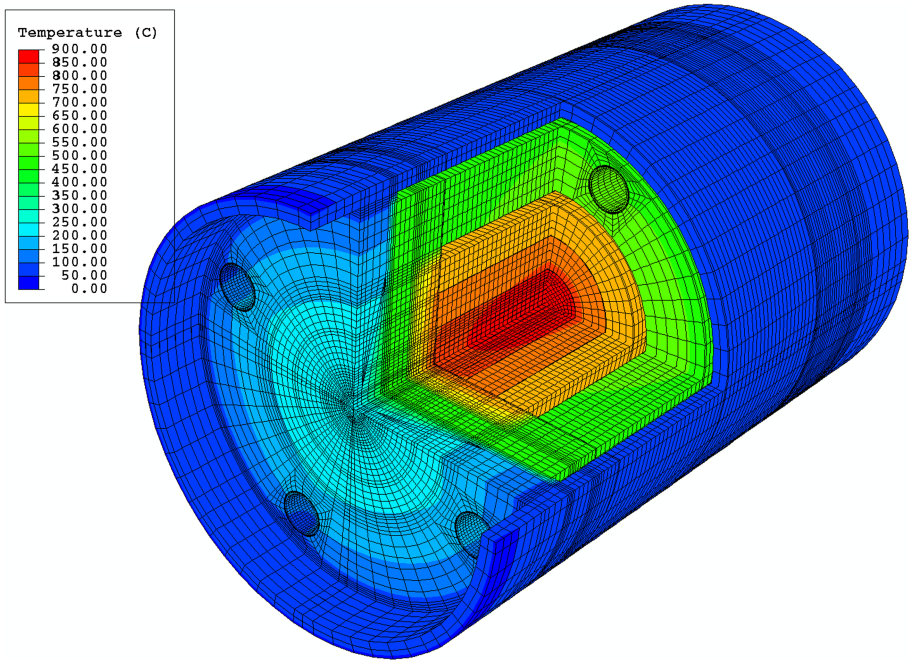

Fig. 12 Cutaway view temperature contours (°C) of capsule 12

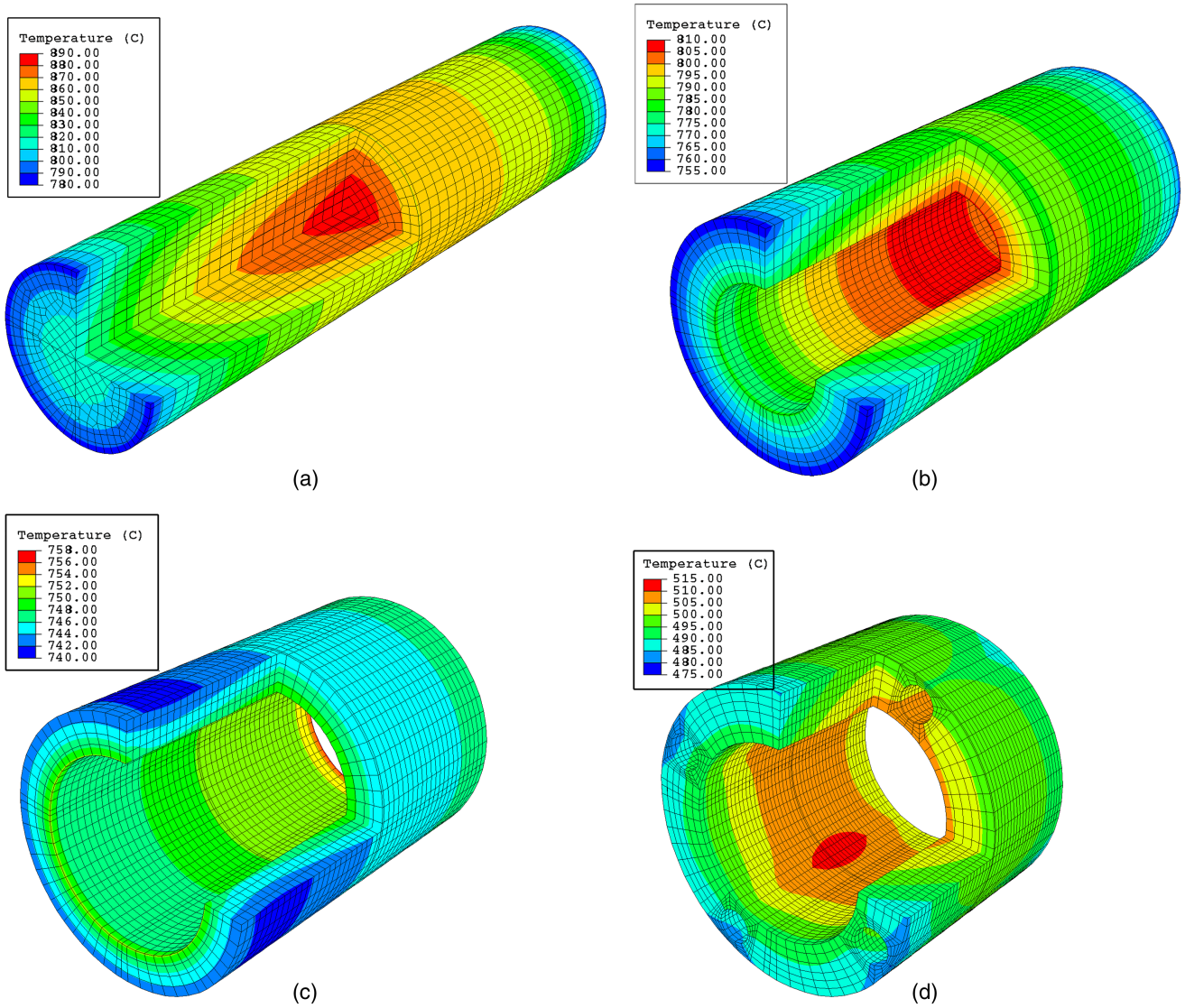

Fig. 13 Temperature contours (°C) of (*a*) compacts, (*b*) matrix, (*c*) graphite sleeve, and (*d*) graphite sink

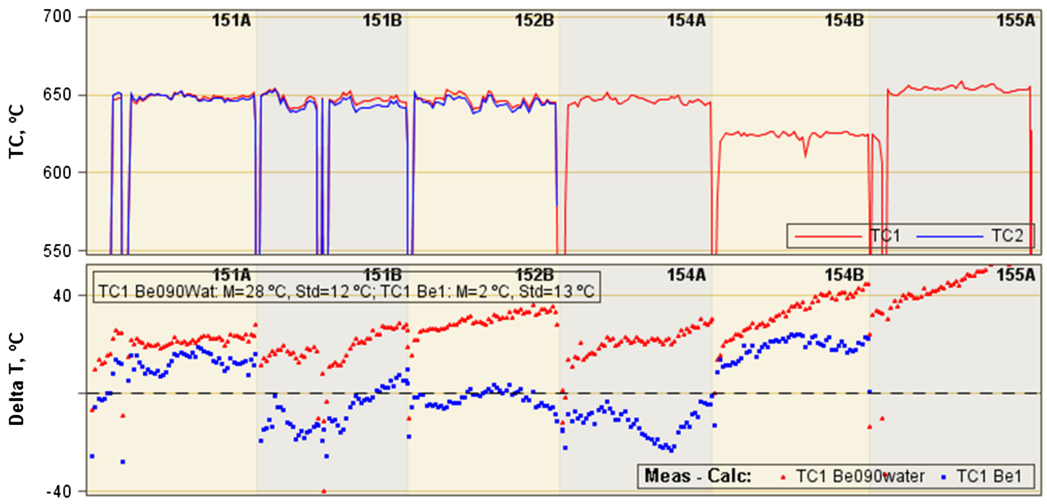

Fig. 14 Capsule 2 temperature (°C) history plot of actual TC measurements (panel 1) and difference between TCs and simulations (panel 2) for six ATR cycles

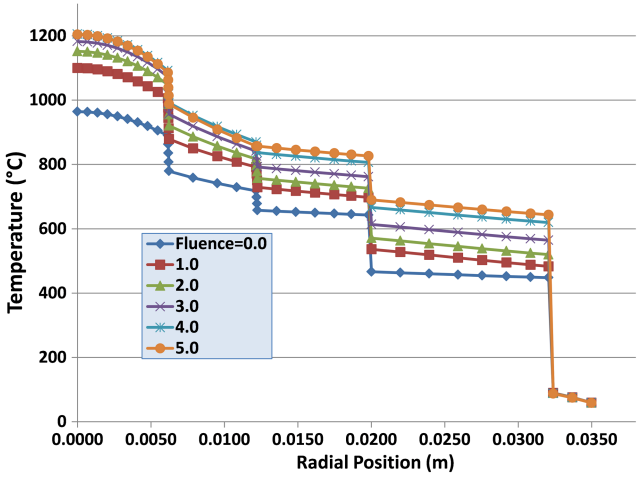

Fig. 15 Radial temperature (°C) profile for constant heat rate and constant neon fraction varying with fluence (not realistic)

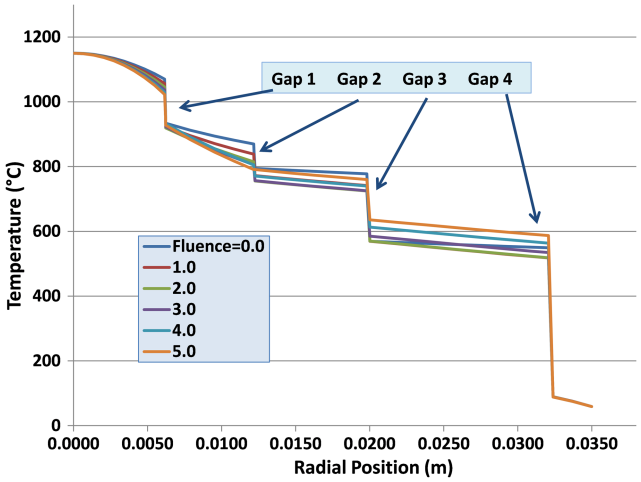

Fig. 16 Radial temperature (°C) profile for constant heat rate and constant peak centerline temperature varying with fluence

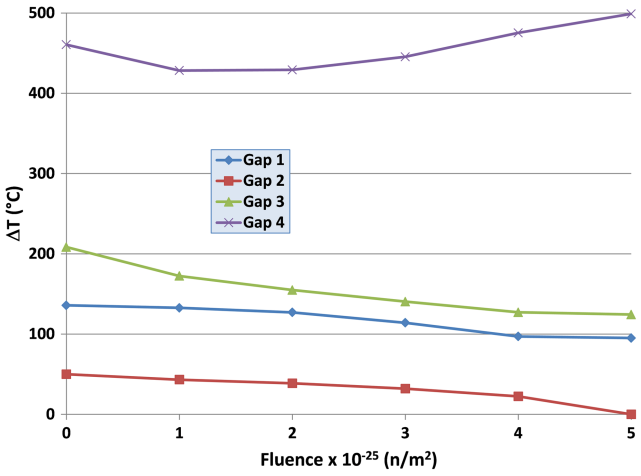

Fig. 17 Temperature difference (°C) across all four gaps varying with fluence and neon fraction to maintain constant peak fuel temperature

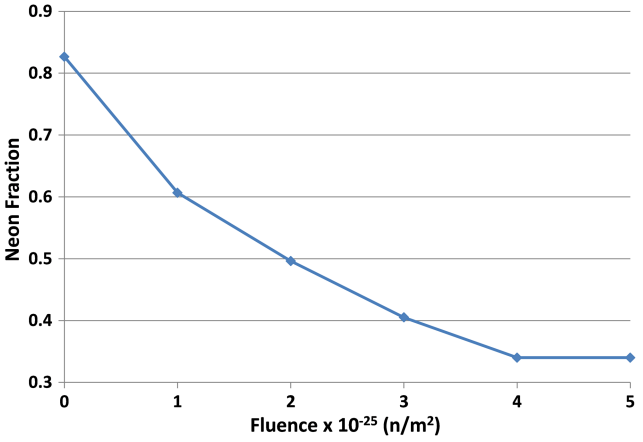

Fig. 18 Neon fraction versus fluence for constant heat rate and peak centerline temperature

cause some graphite layers to move by a very small amount toward one direction or another inside the annulus. An ongoing effort is being made to finalize the modeling technique necessary to minimize the difference between measured and calculated TCs. The temperature difference between the measured minus calculated has a maximum of 20°C as the model is doing a good job of predicting the TCs.

A radial temperature profile of capsule 5 is presented in Fig. 15 varying with neutron fast fluence for constant heat rates from the third cycle, day 8 with a constant neon fraction of 0.5. Nearly a 250°C centerline temperature difference is observed between the start of irradiation and a fast neutron fluence of 5.0×10^{25} n/m^2, $E_n > 0.18$ MeV. This occurs as the conductivity of the graphite decreases as irradiation progresses and is most notable in the matrix ring (second layer, next to compact). Gap 4 is also growing, causing an increasing temperature drop across the gap. This situation shown in Fig. 15 is unrealistic as the heat rate decreases with irradiation, and the gas mixture would be adjusted so as to maintain a constant TC reading but was included to show the sensitivity to fluence. In order to maintain control of the experiment, the entire north-east lobe power increases.

Referring to Fig. 15, a fluence of 0.0 has the lowest peak centerline temperature, whereas a fluence of 5.0 has the highest due to lower thermal conductivity and larger outer gap (gap 4). One interesting note is that gap 2 closes due to neutron shrinkage differences in the graphite and matrix for a fluence of 5.0. Figures 16–18 show results with a different set of runs performed with varying neon fraction in order to maintain the peak centerline temperature constant at 1150°C. Figure 16 shows gap 2 closing at a fluence of 5.0. Notice the temperature gradient in matrix material varying with fluence.

Figure 17 shows the temperature difference across all four gaps for the scenario with constant peak fuel centerline temperature. Gaps 1, 2, and 3 all have a ΔT that decreases with fluence. Gap 3 is the only graphite-graphite material of the four gaps, meaning that the dimensional change is constant for both materials. Gap 4 has ΔT increasing as the graphite shrinks away from the stainless steel capsule wall, except for a fluence of zero. The ΔT for gap 4 initially decreases due to the drastic change in the graphite conductivity between a fluence of 0 and 1.0.

Figure 18 shows the neon fraction varying with fluence for constant heat rate and constant fuel centerline temperature. As the outer gas gap grows, the neon fraction decreases in order to maintain constant temperature. Again, at a fluence of 5.0, gap 2 closes and causes the necessary neon fraction to be constant between a fluence value of 4.0 and 5.0.

4 Conclusions

Daily as-run thermal analysis has been performed for the AGR-3/4 fuel experiment for all 12 capsules during the first six ATR irradiation cycles of the experiment. A variable gas-gap model changing with fast neutron fluence was implemented. A 3-D finite-element heat transfer model was created to simulate this experiment in the ATR. Volumetric heat rates and fast neutron fluence were imported from a daily as-run detailed physics analysis. Thermal conductivity of the fuel compacts and graphite holders varied with fluence and temperature. Daily helium–neon gas mixtures were implemented into 12 models. Temperature contours of various components have been presented. Daily history plots of actual TC measurements have been compared to simulated results with these models for all 12 capsules for the first three cycles. The temperature predictions appear to correlate fairly closely with the actual TC measurements. The goal of these predictions is to be able to adjust the TC set points as the fuel burns during the experiment so as to maintain constant fuel temperatures.

Acknowledgment

This work was supported by the U.S. Department of Energy, NGNP Program, Idaho Operations Office Contract DE-AC07-05ID14517.

Funding also was supported by the U.S. Department of Energy, NGNP Program, Idaho Operations Office Contract DE-AC07-05ID14517.

Nomenclature

A = radiation surface area
dpa = displacements per atom
F_{12} = view factor from surface 1 to 2
k = thermal conductivity, $W/m \cdot K$
MeV = million electron volts
MW = molecular weight
$\dot{q}$ = volumetric heat rate, W/m^3
T = temperature
x, y, z = Cartesian coordinates
Γ = fast neutron fluence, n/m^2
μ = molecular viscosity, $kg/m \cdot s$
σ = Stefan–Boltzmann constant, $W/m^2 K^4$
ε = emissivity

Subscripts

DNE = dido nickel equivalent
irr = irradiated
0 = unirradiated

References

[1] Hawkes, G. L., Sterbentz, J. W., Maki, J. T., and Pham, B. T., 2012, "Daily Thermal Predictions of the AGR-1 Experiment With Gas Gaps Varying With Time," ICAPP 2012 Conference, Chicago, IL, Jun. 2012, Paper No. 12111.

[2] Hawkes, G. L., Sterbentz, J. W., and Pham, B. T., 2015, "Thermal Predictions of the AGR-2 Experiment With Variable Gas Gaps," Nucl. Technol., **190**(3), 10.1382/NT14-73.

[3] Dassault SystŁmes, 2012, ABAQUS Version 6.11-1, www.simulia.com or www.abaqus.com, Providence, RI.

[4] Sterbentz, J. W., Hawkes, G. L., Maki, J. T., and Petti, D. A., 2010, "Monte Carlo Depletion Calculation for the AGR-1 TRISO Particle Irradiation Test," ANS Annual Conference, San Diego, CA, Jun. 2010, Paper No. 1308.

[5] Gontard, R., and Nabielek, H., 1990, "Performance Evaluation of Modern HTR TRISO Fuels," Forschungszentrum Jülich GmbH, Germany, *HTA-IB-05/90*, July 31.

[6] Gonzo, E. E., 2002, "Estimating Correlations for the Effective Thermal Conductivity of Granular Materials," Chem. Eng. J., **90**(3), pp. 299–302.

[7] Windes, W., 2012, "Data Report on Post-Irradiation Dimensional Change in AGC-1 Samples," Idaho National Laboratory, Idaho Falls, ID, *INL/EXT-12-26255*.

[8] Snead, L. L., and Burchell, T. D., 1995, "Reduction in Thermal Conductivity Due to Neutron Irradiation," Proceedings of the 22nd Biennial Conference on Carbon, Extended Abstracts, The American Carbon Society, pp. 774–775.

[9] Sterbentz, J. W., 2009, "Fast Flux to DPA Multiplier," E-mail communication to G. L. Hawkes, Aug. 5.

[10] Kestin, J., Knierim, K., Mason, E. A., Najafi, B., Ro, S. T., and Waldman, M., 1984, "Equilibrium and Transport Properties of the Noble Gases and Their Mixtures at Low Density," J. Phys. Chem, **13**(1), pp 229–303.

[11] Demkowicz, P., Cole, L., Ploger, S., Winston, P., Pham, B., and Abbott, M., 2011, "AGR-1 Irradiated Test Train Preliminary Inspection and Disassembly First Look," Idaho National Laboratory, Idaho Falls, ID, *INL/EXT-10-20722*.

[12] Windes, W., 2012, "Data Report on Post-Irradiation Dimensional Change in AGC-1 Samples," Idaho National Laboratory, Idaho Falls, ID, *INL/EXT-12-26255*.

[13] Hrovat, M. F., Grosse, K-H., and Seemann, R., 2008, "Fabrication, Properties and Irradiation Performance of Molded Block Fuel Elements for HTGRs," Proceedings of the 4th International Topical Meeting on High Temperature Reactor Technology, Washington, DC, Sept. 28–Oct. 1, ASME, Paper No. HTR2008-58025.

[14] Harmon, D. P., Scott, C. B., and Scheffel, W. J., 1974, "Postirradiation Examination of Peach Bottom Core-2 Fuel Element C11-07," General Atomic Company, San Diego, CA, *Report No. GA-A12460*, Aug. 6.